Anterior segment imaging with Spectral OCT system using a high-speed CMOS camera

Ireneusz Grulkowski[1], Michalina Gora[1], Maciej Szkulmowski[1], Iwona Gorczynska[1], Daniel Szlag[1], Susana Marcos[2], Andrzej Kowalczyk[1], and Maciej Wojtkowski[1,*]

[1]Institute of Physics, Nicolaus Copernicus University, ul. Grudziądzka 5/7, PL-87-100 Toruń, Poland
[2]Visual Optics and Biophotonics Lab, Instituto de Óptica "Daza de Valdés", Consejo Superior de Investigaciones Científicas, C/ Serrano 121, 28006 Madrid, Spain
[*]Corresponding author: maciej.wojtkowski@fizyka.umk.pl

Abstract: We describe a new ultrahigh speed Spectral OCT instrument making use of a CMOS camera and demonstrate high quality *in vivo* imaging of the anterior segment of the human eye. The high flexibility of the designed imaging system allows a wide range of imaging protocols. Two- and three-dimensional high quality OCT images of the cornea, the anterior chamber and the crystalline lens are presented. A high acquisition rate, up to 135,000 A-scans/second enables three-dimensional reconstruction of the anterior segment during lenticular accommodation, blinking and pupillary reaction to light stimulus. We demonstrate OCT tomographic real time imaging of the lens dynamics during accommodation and high quality OCT cross-sectional images of the entire anterior segment of the eye from the cornea up to posterior part of the crystalline lens.

OCIS codes: (170.4500) Optical coherence tomography; (170.3880) Medical and biological imaging; (170.4470) Ophthalmology.

References and links

1. D. Huang, E. A. Swanson, C. P. Lin, J. S. Schuman, W. G. Stinson, W. Chang, M. R. Hee, T. Flotte, K. Gregory, C. A. Puliafito, and J. G. Fujimoto, "Optical coherence tomography," Science **254**, 1178-1181 (1991).
2. A. F. Fercher, C. K. Hitzenberger, G. Kamp, and S. Y. Elzaiat, "Measurement of intraocular distances by backscattering spectral interferometry," Opt. Commun. **117**, 43-48 (1995).
3. A. M. Zysk, F. T. Nguyen, A. L. Oldenburg, D. L. Marks, and S. A. Boppart, "Optical coherence tomography: a review of clinical development from bench to bedside," J. Biomed. Opt. **12**, 051403 (2007).
4. W. Drexler, "Ultrahigh-resolution optical coherence tomography," J. Biomed. Opt. **9**, 47-74 (2004).
5. Z. Chen, T. E. Milner, D. Dave, and J. S. Nelson, "Optical Doppler tomographic imaging of fluid flow velocity in highly scattering media," Opt. Lett. **22**, 64-66 (1997).
6. Z. P. Chen, T. E. Milner, S. Srinivas, X. J. Wang, A. Malekafzali, M. J. C. vanGemert, and J. S. Nelson, "Noninvasive imaging of in vivo blood flow velocity using optical Doppler tomography," Opt. Lett. **22**, 1119-1121 (1997).
7. M. Szkulmowski, A. Szkulmowska, T. Bajraszewski, A. Kowalczyk, and M. Wojtkowski, "Flow velocity estimation using joint Spectral and Time domain Optical Coherence Tomography," Opt. Express **16**, 6008-6025 (2008).
8. U. Morgner, W. Drexler, F. X. Kartner, X. D. Li, C. Pitris, E. P. Ippen, and J. G. Fujimoto, "Spectroscopic optical coherence tomography," Opt. Lett. **25**, 111-113 (2000).
9. B. E. Applegate, C. Yang, and J. Izatt, "Theoretical comparison of the sensitivity of molecular contrast optical coherence tomography techniques," Opt. Express **13**, 8146-8163 (2005).
10. J. A. Izatt, M. D. Kulkami, S. Yazdanfar, J. K. Barton, and A. J. Welch, "In vivo bidirectional color Doppler flow imaging of picoliter blood volumes using optical coherence tomography," Opt. Lett. **22**, 1439-1441 (1997).
11. J. F. De Boer, T. E. Milner, M. J. C. van Gemert, and J. S. Nelson, "Two-dimensional birefringence imaging in biological tissue by polarization-sensitive optical coherence tomography," Opt. Lett. **22**, 934-936 (1997).
12. R. Leitgeb, M. Wojtkowski, A. Kowalczyk, C. K. Hitzenberger, M. Sticker, and A. F. Fercher, "Spectral measurement of absorption by spectroscopic frequency-domain optical coherence tomography," Opt. Lett. **25**, 820-822 (2000).

#106214 - $15.00 USD Received 12 Jan 2009; revised 6 Mar 2009; accepted 8 Mar 2009; published 12 Mar 2009

13. G. Hausler and M. W. Lindner, ""Coherence Radar" and "Spectral Radar" - New Tools for Dermatological Imaging," J. Biomed. Opt. **3**, 21-31 (1998).
14. M. Wojtkowski, R. Leitgeb, A. Kowalczyk, T. Bajraszewski, and A. F. Fercher, "In vivo human retinal imaging by Fourier domain optical coherence tomography," J. Biomed. Opt .**7**, 457-463 (2002).
15. S. H. Yun, G. J. Tearney, J. F. de Boer, N. Iftimia, and B. E. Bouma, "High-speed optical frequency-domain imaging," Opt. Express **11**, 2953-2963 (2003).
16. M. Wojtkowski, V. J. Srinivasan, T. H. Ko, J. G. Fujimoto, A. Kowalczyk, and J. S. Duker, "Ultrahigh-resolution high-speed Fourier domain optical coherence tomography and methods for dispersion compensation," Opt. Express **12**, 2404-2422 (2004).
17. M. Wojtkowski, T. Bajraszewski, P. Targowski, and A. Kowalczyk, "Real-time in vivo imaging by high-speed spectral optical coherence tomography," Opt. Lett. **28**, 1745-1747 (2003).
18. R. Huber, M. Wojtkowski, and J. G. Fujimoto, "Fourier Domain Mode Locking (FDML): A new laser operating regime and applications for optical coherence tomography," Opt. Express **14**, 3225-3237 (2006).
19. R. Leitgeb, C. K. Hitzenberger, and A. F. Fercher, "Performance of Fourier domain vs. time domain optical coherence tomography," Opt. Express **11**, 889-894 (2003).
20. J. F. de Boer, B. Cense, B. H. Park, M. C. Pierce, G. J. Tearney, and B. E. Bouma, "Improved signal-to-noise ratio in spectral-domain compared with time-domain optical coherence tomography," Opt. Lett. **28**, 2067-2069 (2003).
21. M. A. Choma, M. V. Sarunic, C. H. Yang, and J. A. Izatt, "Sensitivity advantage of swept source and Fourier domain optical coherence tomography," Opt. Express **11**, 2183-2189 (2003).
22. T. Dada, R. Sihota, R. Gadia, A. Aggarwal, S. Mandal, and V. Gupta, "Comparison of anterior segment optical coherence tomography and ultrasound biomicroscopy for assessment of the anterior segment," J. Cataract Refract. Surg. **33**, 837-840 (2007).
23. A. Konstantopoulos, P. Hossain, and D. F. Anderson, "Recent advances in ophthalmic anterior segment imaging: a new era for ophthalmic diagnosis?," Br. J. Ophthalmol. **91**, 551-557 (2007).
24. W. Nolan, "Anterior segment imaging: ultrasound biomicroscopy and anterior segment optical coherence tomography," Curr. Opin. Ophthalmol. **19**, 115-121 (2008).
25. W. J. Dupps, "Anterior segment imaging: New milestones, new challenges," J. Cataract. Refract. Surg. **32**, 1779-1783 (2006).
26. P. Rosales, M. Dubbelman, S. Marcos, and R. van der Heijde, "Crystalline lens radii of curvature from Purkinje and Scheimpflug imaging," J. Vision **6**, 1057-1067 (2006).
27. J. A. Izatt, M. R. Hee, E. A. Swanson, C. P. Lin, D. Huang, J. S. Schuman, C. A. Puliafito, and J. G. Fujimoto, "Micrometer-scale resolution imaging of the anterior eye in vivo with optical coherence tomography," Arch. Ophthalmol. **112**, 1584-1589 (1994).
28. G. Baikoff, E. Lutun, and C. Ferraz, "Static and dynamic analysis of the anterior segment with optical coherence tomography," J. Cataract Refract. Surg. **30**, 1843-1850 (2004).
29. C. K. Leung, W. M. Chan, C. Y. Ko, S. I. Chui, J. Woo, M. K. Tsang, and R. K. Tse, "Visualization of anterior chamber angle dynamics using optical coherence tomography," Ophthalmology **112**, 980-984 (2005).
30. S. Radhakrishnan, A. M. Rollins, J. E. Roth, S. Yazdanfar, V. Westphal, D. S. Bardenstein, and J. A. Izatt, "Real-time optical coherence tomography of the anterior segment at 1310 nm," Arch. Ophthalmol. **119**, 1179-1185 (2001).
31. J. J. Kałużny, M. Wojtkowski, and A. Kowalczyk, "Imaging of the anterior segment of the eye by Spectra Optical Coherence Tomography," Optica Applicata **32**, 581-589 (2002).
32. M. Wojtkowski, T. Bajraszewski, I. Gorczynska, P. Targowski, A. Kowalczyk, W. Wasilewski, and C. Radzewicz, "Ophthalmic imaging by spectral optical coherence tomography," Am. J. Ophthalmol. **138**, 412-419 (2004).
33. B. J. Kałużny, A. Szkulmowska, M. Szkulmowski, T. Bajraszewski, A. Wawrocka, M. R. Krawczynski, A. Kowalczyk, and M. Wojtkowski, "Granular corneal dystrophy in 830-nm Spectral Optical Coherence Tomography," Cornea **27**, 830-832 (2008).
34. B. J. Kaluzny, J. J. Kaluzny, A. Szkulmowska, I. Gorczynska, M. Szkulmowski, T. Bajraszewski, M. Wojtkowski, and P. Targowski, "Spectral Optical Coherence Tomography: A Novel Technique for Cornea Imaging," Cornea **25**, 960-965 (2006).
35. B. J. Kaluzny, J. J. Kaluzny, A. Szkulmowska, I. Gorczynska, M. Szkulmowski, T. Bajraszewski, P. Targowski, and A. Kowalczyk, "Spectral optical coherence tomography: a new imaging technique in contact lens practice," Ophthalmic Physiol. Opt. **26**, 127-132 (2006).
36. V. Christopoulos, L. Kagemann, G. Wollstein, H. Ishikawa, M. L. Gabriele, M. Wojtkowski, V. Srinivasan, J. G. Fujimoto, J. S. Duker, D. K. Dhaliwal, and J. S. Schuman, "In vivo corneal high-speed, ultra high-resolution optical coherence tomography," Arch. Ophthalmol. **125**, 1027-1035 (2007).
37. B. J. Kaluzny, W. Fojt, A. Szkulmowska, T. Bajraszewski, M. Wojtkowski, and A. Kowalczyk, "Spectral optical coherence tomography in video-rate and 3D imaging of contact lens wear," Optom. Vis. Sci. **84**, 1104-1109 (2007).
38. Y. Yasuno, V. D. Madjarova, S. Makita, M. Akiba, A. Morosawa, C. Chong, T. Sakai, K. P. Chan, M. Itoh, and T. Yatagai, "Three-dimensional and high-speed swept-source optical coherence tomography for in vivo investigation of human anterior eye segments," Opt. Express **13**, 10652-10664 (2005).
39. C. Kerbage, H. Lim, W. Sun, M. Mujat, and J. F. de Boer, "Large depth-high resolution full 3D imaging of the anterior segments of the eye using high speed optical frequency domain imaging," Opt. Express **15**, 7117-7125 (2007).

#106214 - $15.00 USD Received 12 Jan 2009; revised 6 Mar 2009; accepted 8 Mar 2009; published 12 Mar 2009

40. M. V. Sarunic, S. Asrani, and J. A. Izatt, "Imaging the ocular anterior segment with real-time, full-range Fourier-domain optical coherence tomography," Arch. Ophthalmol. **126**, 537-542 (2008).
41. M. Miura, H. Mori, Y. Watanabe, M. Usui, K. Kawana, T. Oshika, T. Yatagai, and Y. Yasuno, "Three-dimensional optical coherence tomography of granular corneal dystrophy," Cornea **26**, 373-374 (2007).
42. M. Miura, K. Kawana, T. Iwasaki, T. Kiuchi, T. Oshika, H. Mori, M. Yamanari, S. Makita, T. Yatagai, and Y. Yasuno, "Three-dimensional anterior segment optical coherence tomography of filtering blebs after trabeculectomy," J. Glaucoma **17**, 193-196 (2008).
43. B. Potsaid, I. Gorczynska, V. J. Srinivasan, Y. Chen, J. Jiang, A. Cable, and J. G. Fujimoto, "Ultrahigh speed spectral / Fourier domain OCT ophthalmic imaging at 70,000 to 312,500 axial scans per second," Opt. Express **16**, 15149-15169 (2008).
44. S. H. Yun, G. J. Tearney, J. F. de Boer, and B. E. Bouma, "Motion artifacts in optical coherence tomography with frequency-domain ranging," Opt. Express **12**, 2977-2998 (2004).
45. M. Szkulmowski, A. Szkulmowska, I. Grulkowski, D. Szlag, A. Kowalczyk, and M. Wojtkowski, Nicolaus Copernicus University, Torun, Poland, are preparing a manuscript to be called "Quantitative flow velocity estimation in complex ambiguity free joint Spectral and Time domain Optical Coherence Tomography".
46. A. Szkulmowska, M. Szkulmowski, A. Kowalczyk, and M. Wojtkowski, "Phase-resolved Doppler optical coherence tomography - limitations and improvements," Opt. Lett. **33**, 1425-1427 (2008).
47. Y. Yasuno, S. Makita, T. Endo, G. Aoki, M. Itoh, and T. Yatagai, "Simultaneous B-M-mode scanning method for real-time full-range Fourier domain optical coherence tomography," Appl. Opt. **45**, 1861-1865 (2006).
48. R. K. K. Wang, "In vivo full range complex Fourier domain optical coherence tomography," Appl. Phys. Lett. **90**, 054103 (2007).
49. American National Standards Institute, *Safe Use of Lasers* (ANSI, 1993).
50. M. Szkulmowski, A. Wojtkowski, T. Bajraszewski, I. Gorczynska, P. Targowski, W. Wasilewski, A. Kowalczyk, and C. Radzewicz, "Quality improvement for high resolution in vivo images by spectral domain optical coherence tomography with supercontinuum source," Opt. Commun. **246**, 569-578 (2005).
51. P. Targowski, W. Gorczynska, M. Szkulmowski, M. Wojtkowski, and A. Kowalczyk, "Improved complex spectral domain OCT for in vivo eye imaging," Opt. Commun. **249**, 357-362 (2005).

1. Introduction

Optical coherence tomography (OCT) is one of the most rapidly developing biomedical imaging modalities. In this technique the structural information is derived from the light backscattered or backreflected at the interfaces between the regions of different optical properties within the object. OCT technique enables two- or three-dimensional (2-D or 3-D) cross-sectional imaging with micrometer resolution [1-4]. Besides morphology, OCT reveals and visualizes such properties of biological objects as velocity of flow (via Doppler effect), birefringence (via polarization changes) and tissue extinction [5-12].

OCT has emerged from low-coherence interferometry [2]. Currently two main detection schemes are used in OCT instrumentation. In the conventional Time-domain OCT (TdOCT), a single in-depth distribution of scatterers (A-scan) is extracted by varying the length of the reference arm [1]. Significantly better performance can be achieved by spectral analysis of interferometric signal recorded as a function of wavelength, which is a basis of Fourier-domain OCT (FdOCT) [2, 13, 14]. In the latter technique, a spectral fringe pattern (chanelled spectrum) is recorded either by a spectrometer with a line-scan camera (Spectral OCT, SOCT) or by a single detector with a rapidly tunable laser as a light source (Swept Source OCT, SSOCT) [15-18]. In FdOCT, a tomogram line is calculated by unevenly sampled Fourier transformation of the recorded fringe pattern. Since this method does not require mechanical depth scanning, it can perform imaging much faster. Another advantage of FdOCT technology is its higher sensitivity, which contributes to higher image quality [19-21].

In both OCT techniques the structure of the test object is imaged in a noninvasive, non-contact way. Due to recent technological advances and extensive clinical studies OCT has attracted a growing interest as a medical diagnostic tool, and has proven especially useful in ophthalmic imaging. As a consequence, several commercial TdOCT and FdOCT instruments have been introduced to the market.

There are few imaging modalities that can perform cross-sectional imaging of anterior segment of the eye. These include slit scanning topography, Scheimpflug imaging, ultrasound biomicroscopy [22-26]. OCT imaging of anterior segment of eye has earned considerable

#106214 - $15.00 USD Received 12 Jan 2009; revised 6 Mar 2009; accepted 8 Mar 2009; published 12 Mar 2009

attention since the first demonstration in 1994 [27], and most of the available commercial devices dedicated strictly to anterior segment imaging are limited to Time-domain OCT method, which is relatively slow [28-30]. The first publication presenting anterior segment imaging with Spectral OCT was published by our group in 2002 [31]. Two years later we presented the first ultrahigh resolution images of human cornea *in vivo* measured by Spectral OCT laboratory system with a supercontinuum light source [32]. Clinical imaging of the anterior segment with high resolution Spectral OCT have proven the applicability of this technique in diagnosis of corneal diseases as well as in monitoring of postoperative healing process [33-36]. Possible applications to optometry such as contact lens fit to and its movement on the eye surface were demonstrated by video-rate and three-dimensional imaging performed with the spectral optical coherence tomography [37]. New tunable light sources have been reported for anterior segment OCT imaging [38-42].

Recently, ultrahigh speed and ultrahigh resolution Spectral OCT imaging using CMOS detector applied to the normal human retina has been demonstrated [43]. Unlike the retina, anterior segment imaging requires covering a much larger volume. The depth of anterior segment is more than 3 mm measured from the apex of the cornea to the anterior surface of the crystalline lens and its diameter is more than 12 mm. The main problem in the anterior segment imaging using Fourier-domain OCT stems from the fact that a considerable part of the signal originates from tilted surfaces of cornea. Under this circumstance the transverse scanning leads to the wash-out effect, which causes a significant signal drop in Spectral OCT devices or resolution decrease in Swept Source OCT systems [44]. To avoid these inconveniences a dense transverse scanning is necessary, which requires ultrahigh speed OCT instrumentation. Unfortunately, dense sampling and large imaging depth results in longer examination time and huge amount of data (1.5 GB). The latter causes practical problems to handle such large volumes of data in current PCs.

The properties of CMOS cameras make them well suited to be used in anterior chamber imaging because one has a possibility of a flexible choice of active pixels influencing both examination time and number of voxels, which is not possible in Spectral OCT systems based on CCD cameras. Using CMOS detector allows to design and construct a spectrometer for Fourier-domain OCT instrument offering much more flexibility of operation [36]. The number of pixels per A-scan can be set for high speed data acquisition yet allowing for large imaging depths and preserving sufficient axial resolution for good quality OCT imaging.

We designed and constructed a new Spectral OCT instrument for high speed imaging of the anterior segment of the human eye *in vivo* using a CMOS camera. In this paper, we demonstrate advantages and limitations of this setup. Line-scan rates as high as 135,000 lines per second allowed us to obtain high-resolution two- and three-dimensional OCT images of the entire cornea and anterior chamber including anterior part of the crystalline lens. The system also enables imaging the full cross-section of the crystalline lens. Due to higher scattering at 840nm the internal structure of the lens can be visualized also in healthy eyes. Additionally, we apply a method for complex conjugate image removal to extend the imaging depth up to 10 mm. Finally, we demonstrate the possibility to perform studies of dynamic processes in the anterior segment in three dimensions and in real time.

2. Experimental setup and Methods

2.1 Comparison of the SOCT system performance with CMOS and CCD cameras

High sensitivity of OCT instruments is a prerequisite to detect extremely low intensities of light backscattered or backreflected from the imaged objects. Sensitivity is defined as a reciprocal of the lowest sample reflectivity, for which power of interferometric signal:

$$Signal = \frac{\rho^2 P_0^2}{N} \gamma_r^2 \gamma_s^2 R_r R_s \tag{1}$$

#106214 - $15.00 USD Received 12 Jan 2009; revised 6 Mar 2009; accepted 8 Mar 2009; published 12 Mar 2009

matches noise i.e. signal-to-noise ratio (SNR) equals 1; where ρ is the efficiency of the optical system including the spectrometer efficiency, P_0 - optical power of the light integrated over the entire spectrum, which is assumed to be a Gaussian function, N - number of pixels (number of samples) of the detector, R_r - reflectivity of reference mirror, R_s - sample reflectivity, γ_s, γ_r – known one-way fiber coupler coupling coefficients. The noise is expressed in terms of the signal variance (σ^2). The main noise sources in OCT systems include:

a) shot noise:

$$\sigma_{sh}^2 = \frac{P_0}{N}\frac{e^-}{T_{\exp}}\gamma_r\gamma_s\rho(R_r + R_s) \tag{2}$$

b) thermal noise:

$$\sigma_{th}^2 = 4k_B T\frac{\Delta f}{R} = \frac{A_{th}}{T_{\exp}}, \qquad \Delta f = \frac{1}{2T_{\exp}}, \quad A_{th} = \frac{2k_B T}{R} \tag{3}$$

where k_B is Boltzmann constant, T - temperature, R - resistance, $T_{\exp}$ - exposure time and Δf - electronic bandwidth of the data acquisition instrumentation;

c) excess intensity noise:

$$\sigma_{ex}^2 = A_{ex}P_0^2\gamma_r^2\ \gamma_s^2 R_{\mathrm{r}}^2 \tag{4}$$

where, A_{ex} – a coefficient describing contribution of different sources of light fluctuations to the excess noise. Assuming the light intensity backreflected from the sample is negligible compared to that in the reference arm, the signal to noise ratio *SNR* of an FdOCT instrument is given by:

$$SNR = 10\cdot\log\left[\frac{\rho^2 P_0^2}{N\left(\sigma_{sh}^2 + \sigma_{th}^2 + \sigma_{ex}^2\right)}\gamma_r^2\gamma_s^2 R_r R_s\right]. \tag{5}$$

In the most desirable situation, the shot noise dominates and one can neglect both thermal and excess noise. However it is not clear if a CMOS camera enables imaging with shot noise limited detection. In order to test the influence of other noise sources on OCT signal acquired with CMOS and CCD detectors we performed a series of experiments using the same OCT laboratory setup and two different detectors. In the first configuration we used the spectrometer with a CCD detector (AViiVA SM2010; e2v technologies plc, UK). In the second setup we utilized a CMOS camera (Basler sprint spL4096-140k; Basler AG, Germany). Both cameras have the same pixel size of 10μm. The CMOS has two lines of detectors. In presented experiments the camera operated in averaging mode between each two vertical pixels. The interferometer was simplified only to 80:20 fiber coupler, collimators, silver mirrors and density filters. Constructed spectrometer enabled in both cases imaging of 186 nm spectral range spanned over 2048 pixels (0,09 nm/pixel; linear dispersion approximately 9 nm/mm). We determined the sensitivity of each setup as a function of the light intensity in the reference arm. Sensitivity was measured by placing a neutral density filter ND 4.0 of well-known optical density (OD) in the object arm. Then, the ratio of the signal peak (after Fourier transformation; *S*) to the noise (standard deviation calculated from 400 FFT bins starting at 400$^{\mathrm{th}}$ pixel; σ) was determined and the sensitivity value was calculated using a well-known formula:

$$\Sigma = 20\cdot\log\left(\frac{S}{\sigma}\right) + 20\cdot OD\,. \tag{6}$$

Measurements were repeated for arbitrarily chosen values of attenuation in the reference arm set by the variable density filter. Attenuation was monitored by measurement of the optical power in the reference arm. This light intensity was later introduced to Eq. (5) via reflection coefficient value R_r of the reference arm. Each measurement was repeated 40 times and S/σ

#106214 - $15.00 USD Received 12 Jan 2009; revised 6 Mar 2009; accepted 8 Mar 2009; published 12 Mar 2009

value was measured. Then mean and standard deviation were calculated. The results obtained are shown in Fig. 1. Experimental data are plotted as squares with dimension corresponding to average value of measured standard deviation. Losses and the same the theoretical shot noise levels in both systems are very similar. Experimental data are plotted as squares with dimension corresponding to average value of measured standard deviation. Losses and the same the theoretical shot noise levels in both systems are very similar.

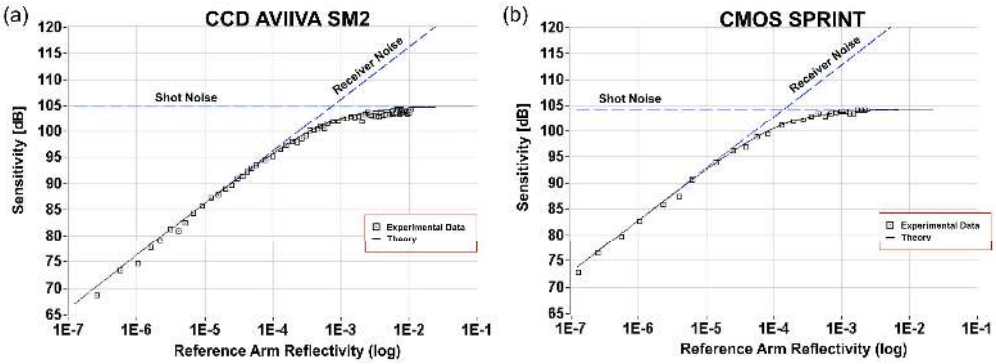

Fig. 1. Sensitivity as a function of the reflectivity of the reference mirror for SOCT systems with CCD (a) and CMOS camera (b) measured for exposure time T_{exp} = 40μs and optical power on the sample P = 1 mW. Theoretical curve (solid line) is fitted to the experimental points using three independent parameters: ρ, A_{th}, A_{ex}. Each parameter was used to calculate corresponding noise contribution. Dashed lines represent hypothetical situations of sensitivity affected by only one noise component.

The experimental sensitivity increases monotonically with the reflectivity of a reference mirror. In Fig. 1, we plotted theoretical computations of contributions of all considered sources of noise influencing the sensitivity, Eq. (5). The theoretical curves (Fig. 1; solid lines) are fitted to experimental data with three independent parameters corresponding to: efficiency of the optical system ρ, and linear coefficients: A_{th}, A_{ex}. To visualize influence of each noise component into the sensitivity for various values of reference reflectivity we plotted sensitivity calculated for each variance (Eqs. (2) – (4)) separately using coefficients found in the fitting procedure (Fig. 2; dashed lines). In both cases the contribution of excess intensity noise is negligible. Therefore, the corresponding plot is out of the range of our graph. The thermal noise dominates for low R_r whereas the shot noise limit (approx. 105 dB) is barely achieved for light intensities, which are close to the saturation limit of both detectors. However, CCD saturates for higher values of the reference arm reflectivity and the same the plateau created by the experimental points is broader.

2.2 The SOCT instrument

The SOCT system based on fiber-optics Michelson interferometer configuration is shown in Fig. 2. The light emitted by a superluminescent diode SLD (λ_0 = 840 nm, $\Delta\lambda$ = 50 nm; Superlum, Ireland) passes through an optical isolator (OFR Inc., USA) and is split by an 80:20 fiber coupler (AC Photonics, Inc., USA) into reference and object arms. The detection arm consists of a custom designed spectrometer containing a collimating lens (Thorlabs, USA), a volume holographic diffraction grating (1800 lines/mm; Wasatch Photonics, USA) and two achromatic doublets (Thorlabs, USA). The spectral interference fringes are captured by a 12-bit line-scan CMOS camera with 4096 pixels (Basler sprint spL4096-140k; Basler AG, Germany) and a frame grabber (PCIe-1429; National Instruments, USA). Transversal scanning is achieved by two galvanometer optical scanners (Cambridge Technology, Inc., USA). The scanners are driven by an analog input/output card (National Instruments, USA). The computer used for the control of the OCT instrument and data acquisition has 2 GB RAM memory, Intel Core 2 Quad processor and 32 bit operation system.

#106214 - $15.00 USD Received 12 Jan 2009; revised 6 Mar 2009; accepted 8 Mar 2009; published 12 Mar 2009

Axial resolution of the SOCT instrument governed solely by the spectral width of the light source is measured to be 6.9 μm in tissue. Transverse resolution depends on focal length of the object lens L4 and is calculated to be 27 μm, which corresponds well to the value measured using a beam analyzer (28 ± 3 μm). The depth of focus is 3.6 mm, and experimentally determined axial imaging range is 5.2 mm in tissue. The sensitivity roll-off over the entire axial imaging range is 19.5 dB.

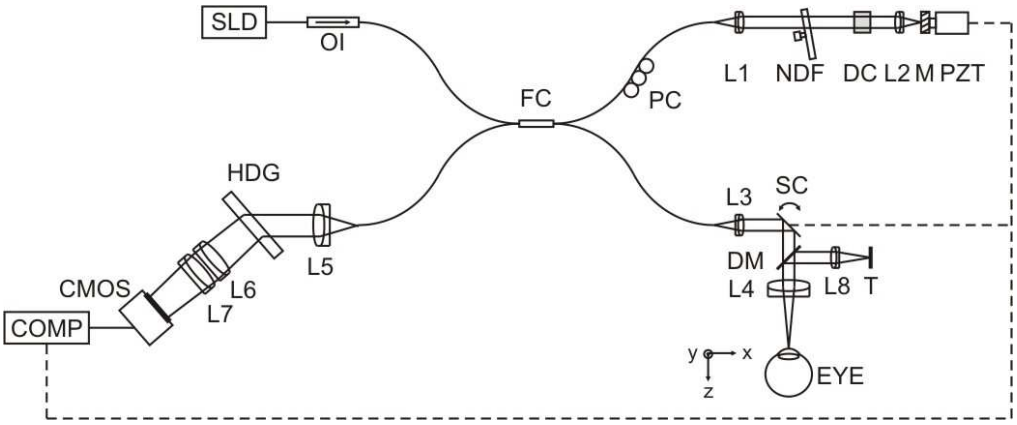

Fig. 2. Experimental SOCT set-up: SLD – superluminescent diode, OI – optical isolator, FC– 80:20 fiber coupler, PC – polarization controller, NDF – neutral density filter, DC – dispersion compensator, L1-L8 – lenses, M – silver mirror, PZT – piezotranslator, SC – galvanometric scanners, DM – dichroic mirror, T – target, HDG – holographic volume diffraction grating, CMOS – linescan camera, COMP – computer.

The sensitivity performance and axial resolution of the instrument is summarized in Table 1. Reduction of the number of active CMOS camera pixels with unchanged configuration of the optical elements in the spectrometer results in truncation of the spectrum (Fig. 3). As a consequence the axial resolution and sensitivity decrease together with reduction of the pixel number from 4096, through 2048 to 1024. The resolution decreases from 6.9 μm to 15.4 μm and the sensitivity drops by 4 dB (if calculated for a given constant exposure time $T_{exp} = 40$ μs). The last column in the Table 1 shows effective sensitivity values taking into account both effects: the shortening of the signal integration time and the truncation of the spectrum.

Table 1. SOCT system parameters for different number of active pixels of the CMOS camera

Number of pixels	Axial resolution [μm]	Sensitivity at T_{exp}= 40 us [dB]	Minimum repetition time $T_{rep}^{(min)}$ [μs]	Sensitivity at $T_{rep}^{(min)}$ [dB]
4096	6.9	102	14.2	97.5
2048	8.7	101	7.8	94
1024	15.4	98	4.7	89

#106214 - $15.00 USD Received 12 Jan 2009; revised 6 Mar 2009; accepted 8 Mar 2009; published 12 Mar 2009

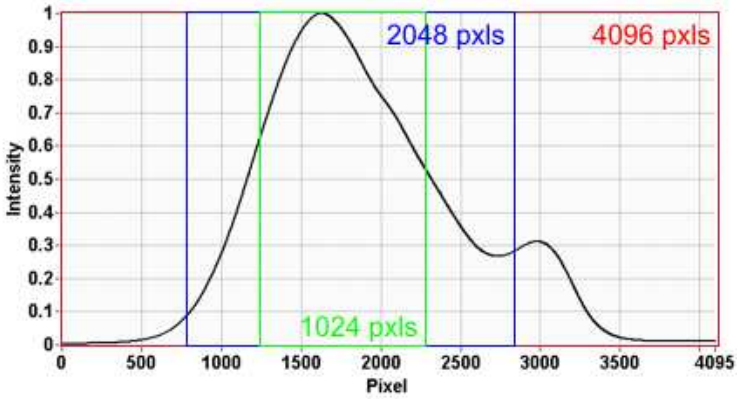

Fig. 3. Spectrum of the light source used in the SOCT system. Areas of interest of the camera capturing 4096, 2048 and 1024 pixels are indicated by red, blue and green rectangles, respectively.

To double the axial measurement range (up to 10 mm) we have implemented a technique of complex conjugate images removal [45] based on a joint Spectral and Time domain OCT (STdOCT) concept previously demonstrated to flow analysis [7, 45, 46]. Our technique requires the optical path difference (OPD) between the arms of the interferometer to be varied at a constant rate during the acquisition of the interferometric signal. Constant OPD change introduces a carrier frequency for every wavenumber along the time axis. In order to generate one A-scan, a two-dimensional Fourier transformation is applied to a small number of acquired spectra (not more than 16). In other words, the signal is transformed from the wavenumber-time space to the depth-velocity space. As a consequence, both complex conjugate images are shifted in opposite directions along v axis. Next for each axial position the maximum amplitude of the signal is detected for positive values of v only.

This method is different from B-M mode proposed by Yasuno et al. [47] and the method proposed by Wang et al. [48] as it does not require a back-transformation step. The computation time is longer, but this drawback can be compensated by an increase in sensitivity caused by more efficient averaging of the noise floor [7, 45].

In our approach the OPD change was carried out by a constant movement of the reference mirror (mounted on a piezotranslator (PZT) - Physik Instrumente GmbH & Co. KG, Germany, controlled by a triangle voltage signal of frequency 12.5 Hz and 10 V peak to peak amplitude) with velocity of 1.5 mm/s.

2.3 Imaging of the eye

OCT imaging was performed on 6 healthy volunteers without pupil dilation. The protocols have been approved by Internal Ethics Committee and the subjects signed a consent form. The power of light incident on the eye was set to 1 mW and for short exposure times met the safety requirements of ANSI standards [49]. As a basis for the patient imaging platform we used the mechanical system of a commercial OCT instrument (SOCT Copernicus; Optopol Techonlogy S.A., Poland). We used various scan protocols designed for imaging of specific features in the anterior chamber. In this paper we are showing examples of two- and three-dimensional images and tomographic movies. The details of specific protocols will be given below. The repetition times ranged from 70 μs in case of high resolution and high definition imaging of the anterior chamber morphology to 7.4 μs for imaging of dynamic processes in the eye. The repetition rates can be easily altered by reducing the number of active pixels of the CMOS camera and/or changing the camera control software settings.

It is important to note that with increasing speeds of the cameras used in spectral OCT the limitation imposed on the imaging protocols is gradually shifted from the imaging time to the size of the data that can be captured with the acquisition system and stored in the hard drives. As an example, dynamic anterior chamber imaging we acquired 12 volumes, 300×100×1024

#106214 - $15.00 USD Received 12 Jan 2009; revised 6 Mar 2009; accepted 8 Mar 2009; published 12 Mar 2009

pixels each, giving ~737 MB of the data. The repetition time was set to 7.4 μs to achieve 91 dB sensitivity. The total imaging time was ~2.66 s. Alternatively a protocol using 2048 pixels in each A-scan, which results in better sensitivity (94 dB; Table 1) and only slightly longer imaging time (~2.8 s) produces a data size of ~1.5 GB, which cannot be handled by the memory allocation of 32 bit Windows XP operating system. Therefore, counter-measures leading to the significant reduction of pixel number were necessary. The problem of memory allocation might be overcome by changing the operating system. However, currently available drivers for the analog input/output card used in the experiment work with 32 bit operating systems.

The data processing was performed using a custom-made software and included background signal removal, remapping the spectra from wavelength to wavenumber space, numerical dispersion compensation and numerical spectral shaping followed by the Fourier transformation [50]. Three-dimensional data were visualized using commercial software (Amira 4.1, Visage Imaging, Inc., USA).

3. Results and discussion

3.1 Evaluation of the instrument performance in imaging of the anterior chamber

As a first evaluation of the imaging capabilities of our instrument we performed high speed imaging of the entire cornea and anterior chamber including anterior part of the crystalline lens. Figure 4 shows OCT images of the healthy eye of the same subject. The aspect ratio in the images was set to take advantage of the higher in-depth resolution comparing with the lateral one. The cross-sections (B-scans) consist of 10,000 A-scans, acquired with two different exposure times: 8.5 μs and 53 μs corresponding to rates of 118,000 A-scans/s and 18,900 A-scans/s, respectively. Anterior segment was imaged with the zero delay (optical path difference OPD = 0) set at the depth of the crystalline lens (Fig. 4(a)) and with the zero delay located in front of the cornea (Fig. 4(b)).

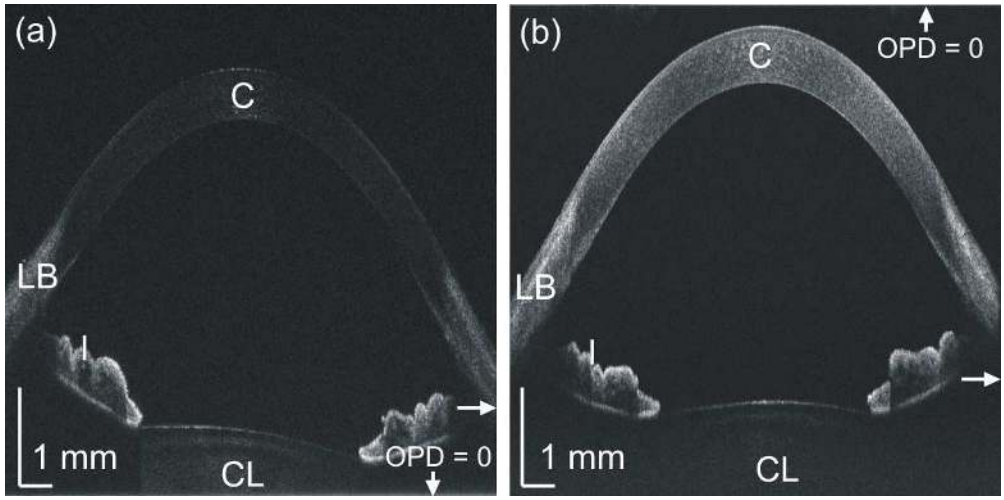

Fig. 4. 2-D OCT imaging of the cornea and anterior chamber: (a) single line exposure time: 8.5 μs, repetition rate: ~117,000 A-scans/s, 10,000×1024 pixels, 15 mm, (b) single line exposure time: 53 μs, repetition rate: ~19,000 A-scans/s, 10,000×4096 pixels, 15 mm. Structural elements including the cornea (C), limbus (LB), iris (I) and the crystalline lens (CL) are visible. Position of zero optical path difference (OPD = 0) is indicated. Horizontal arrows show the position of the focal plane of the imaging lens.

The positions of the focal plane of the imaging lens are indicated by horizontal lines. Imaging with long exposure times, and therefore also high sensitivity, provides, as expected, high quality images. However, the two tomograms show the relevance of sensitivity drop compensation with a correct setting of the zero delay location. Even with six-fold shorter

#106214 - $15.00 USD Received 12 Jan 2009; revised 6 Mar 2009; accepted 8 Mar 2009; published 12 Mar 2009

exposure time, the signal from the crystalline lens is stronger in Fig. 4(a) than in Fig. 4(b). In addition, imaging with higher speed reveals the morphology of the anterior chamber as accurately as imaging with long exposure time despite its lower sensitivity. Structural elements including the cornea, limbus, iris and the lens are clearly visible in both images.

Figure 5 presents an example of high resolution and high quality imaging of a myopic eye fitted with a soft contact lens. The examination was performed with a long exposure time (70 μs). The image (B-scan) contains a large number of A-scans (15,000). The total acquisition time was 1.05 s. The number of pixels in each A-scan was set to 4096 to achieve the axial resolution of 6.9 μm. The soft contact lens appears as a transparent layer on the top of the cornea. The magnified limbal region illustrates the contact lens fitting on the corneal periphery (Fig. 5(b)). A magnified view of the cornea reveals the details of corneal structural elements such as epithelium, Bowman's membrane, stroma and endothelium (Fig. 5(c)).

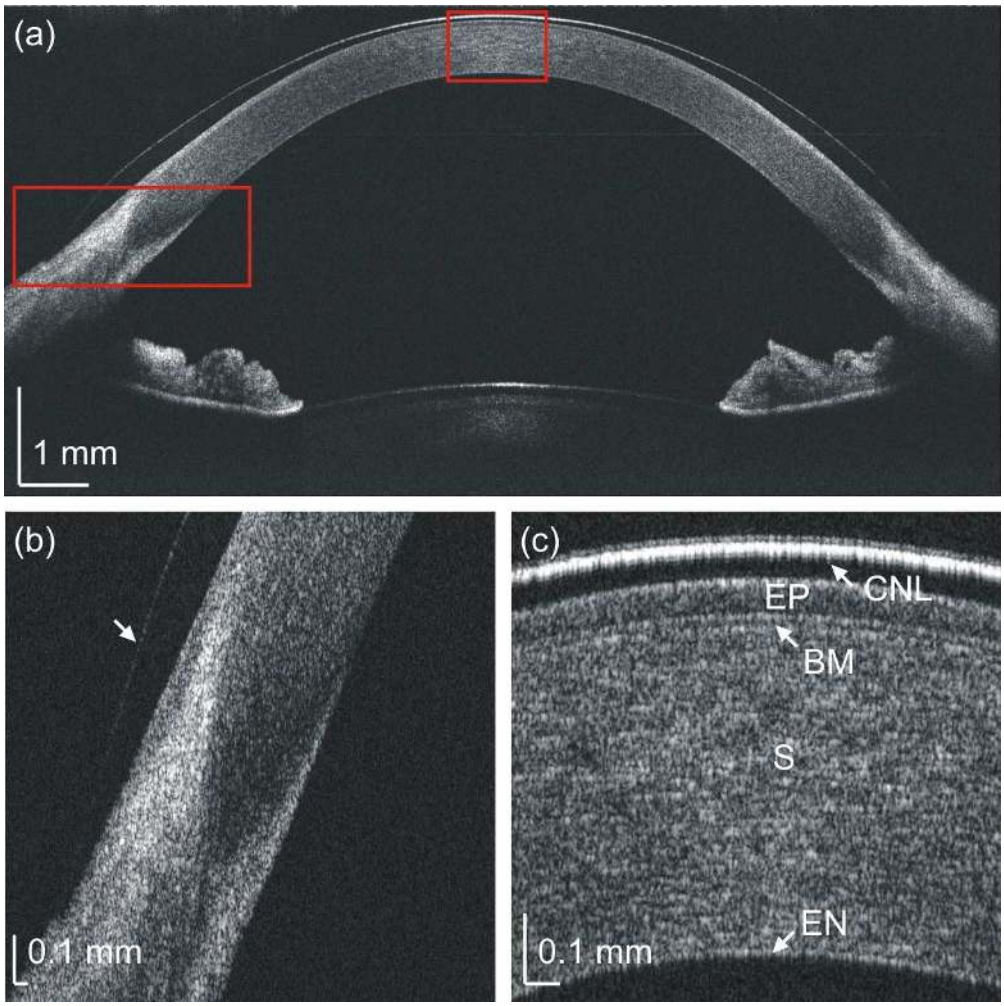

Fig. 5. High resolution and high density imaging of the anterior segment. (a) SOCT cross-sectional image of the anterior segment of myopic eye with a contact lens, single line exposure time 70 μs, repetition rate: ~14,000 A-scans/s, 15,000×4096 pixels, 16 mm. The red rectangles indicate location of the magnified regions shown in panels b and c. (b) Magnification of the limbal region with the contact lens (indicated by the arrow). (c) Magnification of the apex region of the cornea. CNL – contact lens, EP – epithelium, BM – Bowman's membrane, S – stroma, EN – endothelium.

#106214 - $15.00 USD Received 12 Jan 2009; revised 6 Mar 2009; accepted 8 Mar 2009; published 12 Mar 2009

In Fig. 6 we present the three-dimensional image of the anterior chamber of a healthy subject. For the volumetric OCT examination we selected a scan protocol generating 50 B-scans consisting of 1000 A-scans with 1024 pixels in each line. The data set was collected in 0.68 s which corresponds to 13.6 μs exposure time. This protocol allows imaging an area of 15 x 15 mm area of the object. In the example shown in Fig. 6 the cornea and iris along with the upper eyelid and eyelashes are clearly visible. Cross sectional views at any position are available.

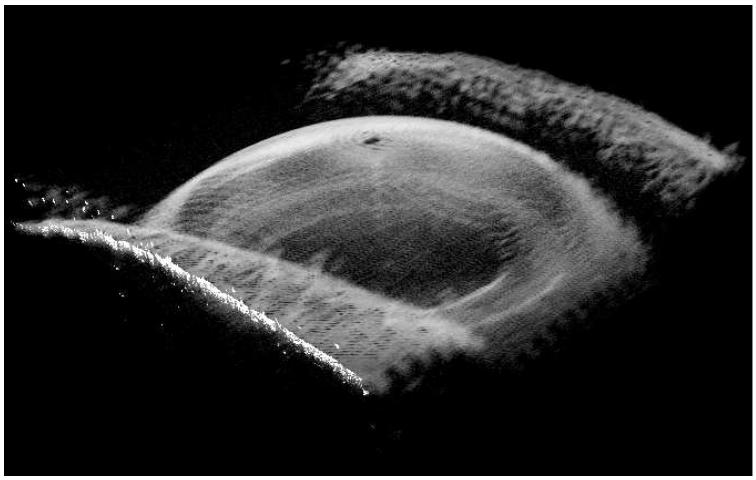

Fig. 6. (Media 1) Movie demonstrating rendered view through the cornea and anterior chamber (1000×50×1024 pixels, 15 mm × 15 mm, single line exposure time 13.6 μs, total measurement time 0.68s).

3.2 Imaging of selected structures in the anterior segment of the eye

Whereas many applications require imaging of the entire anterior segment, other applications will involve focusing on selected structures. Here we show high speed OCT imaging of two important structures: the anterior chamber angle and the crystalline lens.

3.2.1 Cornea and anterior chamber angle

The anterior chamber angle is a region of the eye where a drainage system of aqueous humor is localized. Malfunction of these structures leads to ocular hypertension which in turn can affect the optic nerve. In consequence, evaluation of the anterior chamber angle is key in the diagnosis and monitoring of various eye diseases associated with glaucoma. The geometry and inaccessibility of areas in the proximity of corneo-scleral junction make it challenging to image. The sclera is a highly scattering tissue and therefore limits the light penetration into the iridocorneal angle. The scattering properties depend on the wavelength of light. There is general agreement that light centered at 1300 nm is most suitable for the examination of the anterior chamber due to relatively high penetration of this light through the sclera [39], as the scattering at the ~800 nm wavelength is considerably higher. Figure 7 shows images of the anterior chamber angle in two young subjects (ages 34 and 24 years), collected with our OCT instrument operating at 840 nm. Also here the aspect ratio in the images was adjusted to take the full advantage of almost four times higher axial resolution than the lateral one. The details of the scanning protocols are given in the figure legend. OCT cross-sections in panels 7(a) and 7(b) show a large inter-subject variability in biometry, corneal shape and anterior chamber angle. Although the lateral size is comparable in both eyes, anterior chamber depth (from the corneal apex to the anterior lens surface) differs in 0.75 mm. The cornea appears slightly thinner in the eye shown in panel 7(b) and the length of the limbal part is shorter.

In panel 7(a) the sclera projects a shadow on the anterior chamber angle, which is characteristic of OCT instruments operating at ~800 nm wavelength ranges [29]. This

#106214 - $15.00 USD Received 12 Jan 2009; revised 6 Mar 2009; accepted 8 Mar 2009; published 12 Mar 2009

drawback can be overcome by increasing transverse scanning density and changing the orientation of the examined eye. This procedure enables visualization of the iris up to the sclera as demonstrated in panels 7(c) and 7(d). Also here ontogenetic differences are noticeable in the shape of the limbus.

Due to the reduced scleral thickness at the iridocorneal angle light penetration was sufficient to image the entire depth of the chamber angle and clearly visualize the limbus and the junction between sclera and conjunctiva.

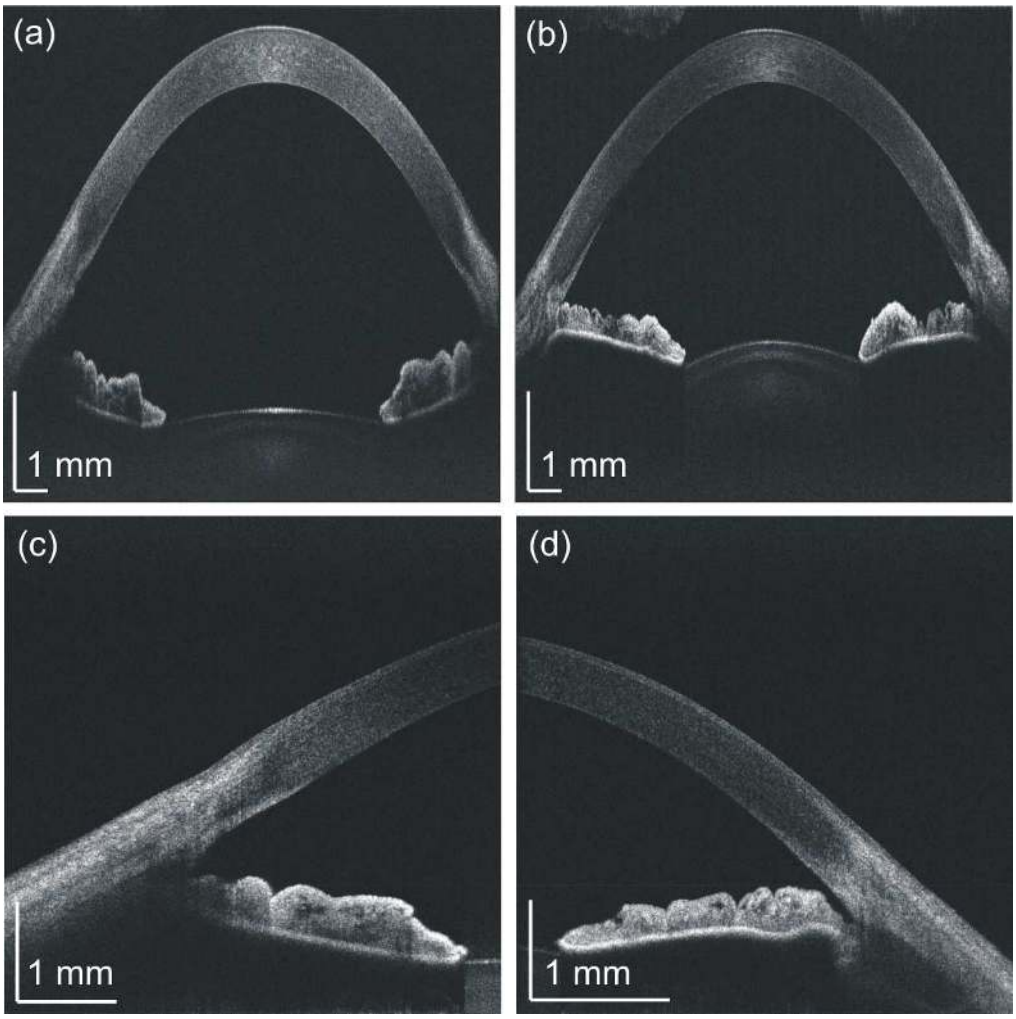

Fig. 7. OCT imaging of the anterior segment of two subjects: (a) subject 1, single line exposure time 43 μs, repetition rate: ~23,000 A-scans/s 10,000×4096 pixels, 15 mm, (b) subject 2, single line exposure time 43 μs, 10,000×4096 pixels, 15 mm. Tomograms of the iridocorneal angle: (c) the same subject as in Fig. 7(a), single line exposure time 50 μs, repetition rate: 20,000 A-scans/s, 10,000×4096 pixels, 5 mm, (d) the same subject as in Fig. 7(b), single line exposure time 50 μs, repetition rate: 20,000 A-scans/s 10,000×4096 pixels, 7 mm.

Our instrument also allows capturing 3-D images of the corneo-scleral junction region. Figure 8 shows a rendered view of the three-dimensional data acquired at the anterior chamber angle of the subject presented in Figs. 7(b) and 7(d).

#106214 - $15.00 USD Received 12 Jan 2009; revised 6 Mar 2009; accepted 8 Mar 2009; published 12 Mar 2009

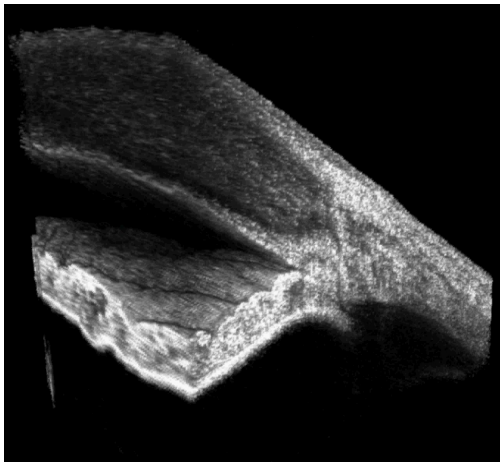

Fig. 8. (Media 2) Movie presenting 3-D imaging of the iridocorneal angle. Volumetric data was obtained with 50 μs single line exposure time, repetition rate: ~20,000 A-scans/s. Data set consisting of 1000×50×4096 pixels was acquired in 4 mm × 3 mm area of the anterior chamber angle.

3-D images reveal the pattern of radial streaks on the iris. The conjunctiva is also clearly visible on top of the sclera. The blurry mass may correspond to the cilliary body.

3.2.2 Crystalline lens

OCT imaging of the crystalline lens is challenging due to its considerable thickness ranging from 3.5 mm to 4.8 mm and its high transparency. In contrast to the imaging of the corneo-scleral junction higher scattering offered by 840 nm can help in visualization of healthy crystalline lenses. Figures 9(a) – 9(c) show cross-sectional SOCT images of crystalline lens of a 26-year old subject. Images were collected over the 8 mm transverse scanning range with 10,000 A-scans, 4096 pixels each. The repetition rates varied from 66,000 A-scans/s to 23,000 A-scans/s. This experiment was performed to determine the shortest repetition (and acquisition) time necessary to get a good quality lens image. For assessing the shape of the anterior capsule and its thickness only, an exposure time of 15 μs is sufficient. Longer exposure times are necessary to unveil the internal structure of the lens and to image the posterior surface.

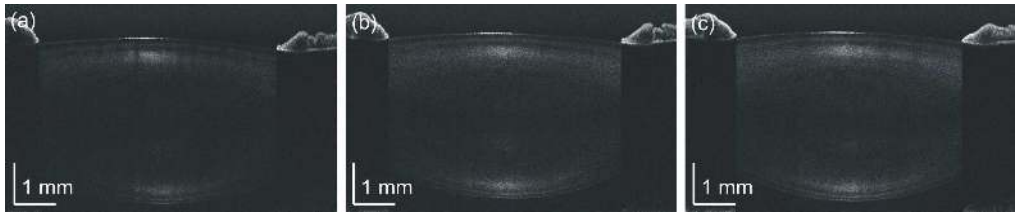

Fig. 9. Cross-sectional images of the crystalline lens obtained with different single line exposure times: 15 μs (panel a), 33 μs (panel b), 43 μs (panel c). The two dimensional data consists of 10,000×4096 pixels in all three cases.

Figure 10(a) shows an image of a crystalline lens in a 30-year old subject obtained with high transverse scanning density (15,000 A-scans in 9 mm). Under these imaging conditions, it is possible to easily distinguish characteristic structures of crystalline lens morphology such as capsule, cortex and nucleus.

#106214 - $15.00 USD Received 12 Jan 2009; revised 6 Mar 2009; accepted 8 Mar 2009; published 12 Mar 2009

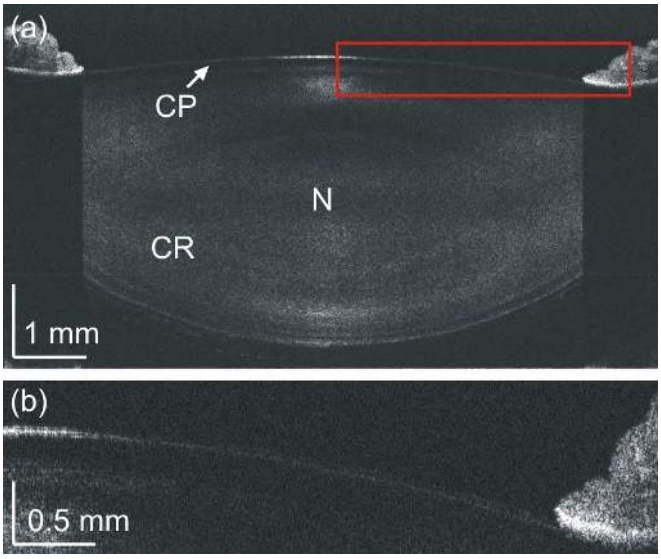

Fig. 10. Cross-sectional image of the crystalline lens: single line exposure time 70 μs, transverse scanning density 15,000 A-scans per 9 mm; 4096 pixels in each A-scan. The red rectangle in panel (a) indicates the location of the magnified region shown in panel b. The capsule CP, nucleus N and cortex CR are visible.

Using the raster scanning protocol consisting of 80 B-scans, 1000 A-scans each, we have obtained volumetric reconstruction of the crystalline lens (Fig. 11). Despite the highly demanding conditions of large imaging depths and high transparency of the crystalline lens our instrument is capable of providing volumetric data of this structure.

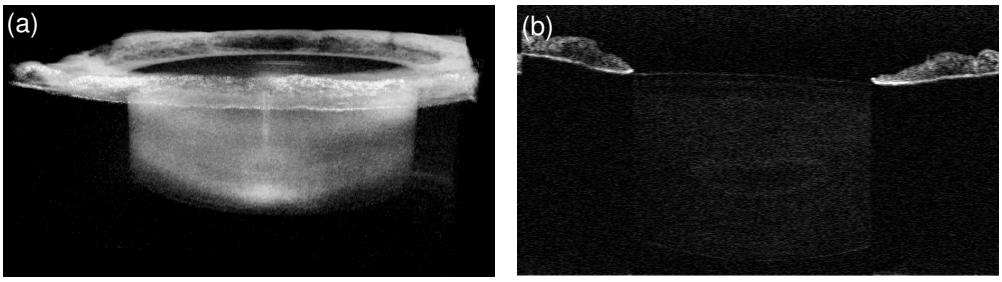

Fig. 11. 3-D visualization of crystalline lens. (a) (Media 3) movie showing rendering of crystalline lens; single line exposure time 70 μs, repetition rate: ~14,000 A-scans/sec, 1000×80×4096 pixels, 9 mm × 9 mm. (b) (Media 4) movie showing a flight-through the crystalline lens: single line exposure time 43 μs, repetition rate: ~22,000 A-scans/s, 1000×50×4096 pixels, 9 mm × 9 mm.

3.3 Imaging of dynamic processes in the anterior chamber

The scan protocols for two- and three-dimensional imaging can be repeated in time. Such approach offers an opportunity to monitor anterior segment of the eye during dynamic processes. The first example (Fig. 12) shows a sequence of cross-sectional images acquired during accommodation of the eye. We recorded successive 80 B-scans (frames), 1000×4096 pixels each, at a constant vertical position at the crystalline lens, during 3.44 s. A target T in the additional channel of the setup (Fig. 2) was moved from a location near the eye to effective infinity inducing an accommodative response in the tested eye. A tomographic movie created from the consecutive B-scans shows a steepening of the anterior lens surface. The posterior surface of the lens seems to be changed to much smaller extend. The movement of the iris is also visible during accommodation. The movie is, to our best knowledge, the first demonstration of OCT imaging of real time lens dynamics during accommodation.

#106214 - $15.00 USD Received 12 Jan 2009; revised 6 Mar 2009; accepted 8 Mar 2009; published 12 Mar 2009

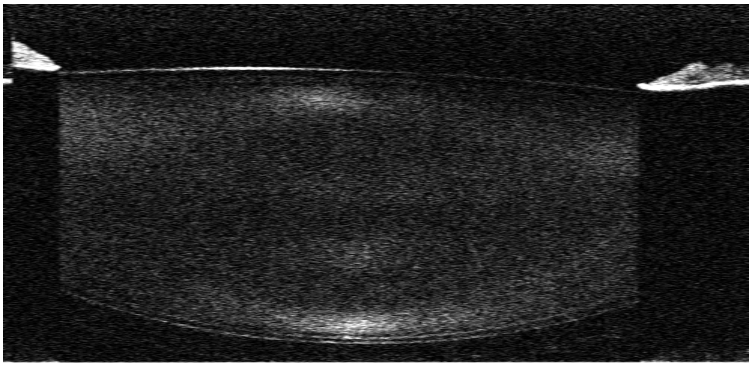

Fig. 12. (Media 5) Movie showing OCT cross-sectional images of crystalline lens during the lenticular accommodation: single line exposure time 43 μs, repetition rate: ~22,000 A-scans/s 1000×4096 pixels (80 frames), 8 mm.

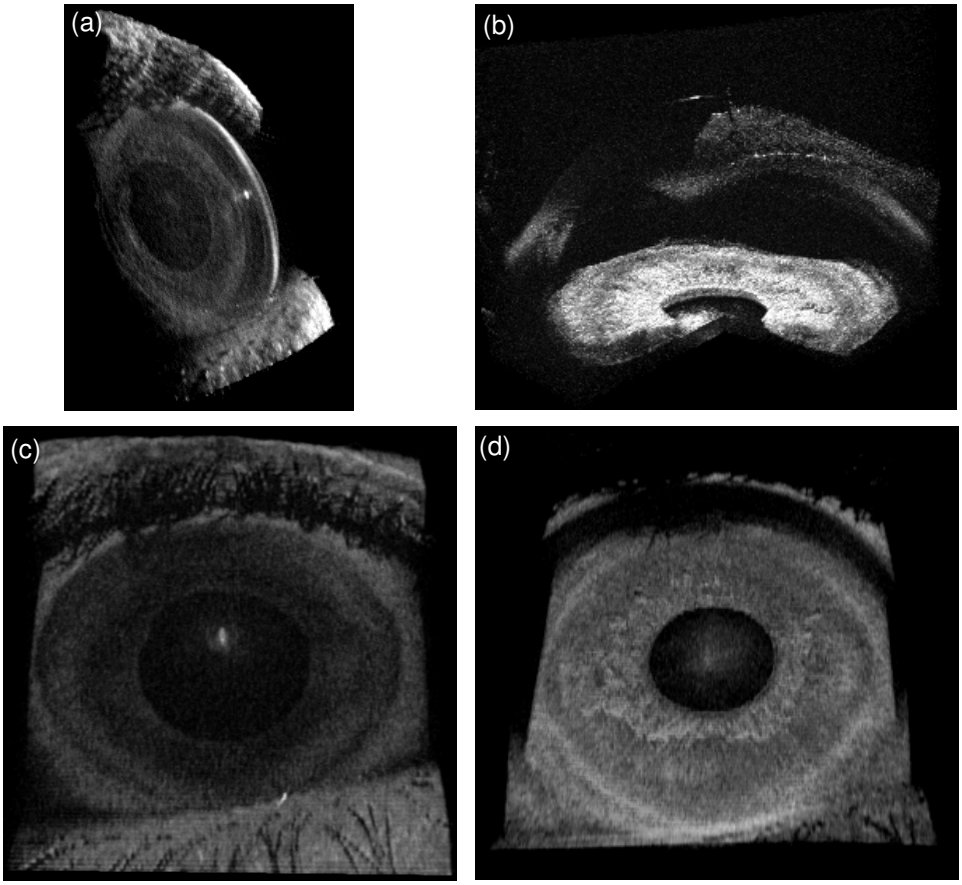

Fig. 13. OCT imaging of eye dynamics, movies showing: (a) (Media 6) eye blinking: 300×100×1024 pixels (12 volumes), 15 mm × 15 mm, (b) (Media 7) reaction to light stimulus: 300×100×1024 pixels (12 volumes), 15 mm × 15 mm, (c) (Media 8) eye blinking presented in *en-face* projection, (d) (Media 9) reaction on light stimulus visualized in *en-face* projection; single line exposure time 7.4 μs, repetition rate: ~ 135,000 A-scans/sec.

The second example demonstrates a capability of our instrument to capture a sequence of OCT volumes. We implemented scan protocols acquiring 12 three-dimensional data sets consisting of 300×100×1024 pixels in horizontal, vertical and axial directions, respectively.

#106214 - $15.00 USD Received 12 Jan 2009; revised 6 Mar 2009; accepted 8 Mar 2009; published 12 Mar 2009

We have reduced the number of active camera pixels to 1024 in order to increase the imaging speed to 135,000 A-scans/s. Each volume was acquired in 222 ms giving 2.7 s total imaging time and a rate of 4.5 volumes/s. Two examples of repeated 3-D OCT imaging are presented in Fig. 13. Panels 13(a) and 13(b) show rendered views of the 3-D data acquired during blinking and reaction of the eye to white-light stimulus, respectively. Visualization of the same dynamic processes in form of *en face* projections are presented in panels 13(c) and 13(d).

3.4 Complex ambiguity free imaging of the entire anterior segment of eye

In order to demonstrate full imaging capabilities of the designed instrument we introduced a technique of complex conjugate image removal based on the STdOCT concept [45]. This technique allowed for imaging of the whole anterior segment of the human eye including the cornea, anterior chamber angle, iris and the entire crystalline lens (Fig. 14).

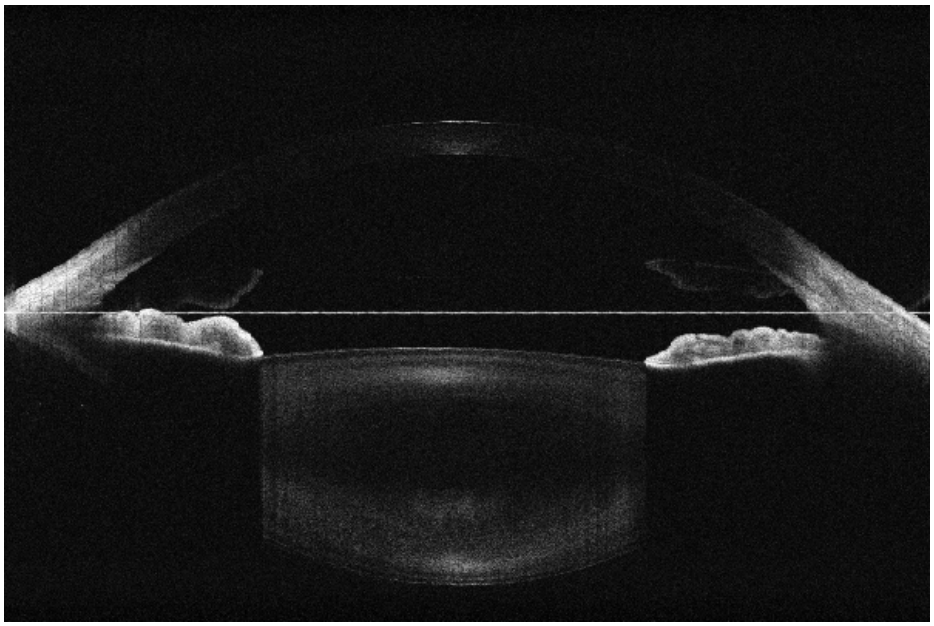

Fig. 14. Full-range complex ambiguity free image of the whole anterior segment of eye: single line exposure time 70 μs, 15,000×4096 pixels, 16 mm.

Ghost images of the iris and sclera visible in the image are caused by limited dynamic range of the method. Small wrinkles noticeable in the sclera and on the top of the lens are associated with the oscillatory movement of the reference mirror. Both effects can be minimized by further image processing [51].

4. Conclusions

We have presented a new system, which performs ultrahigh speed, high-resolution Spectral OCT imaging of the anterior segment of the human eye based on spectrometer equipped with CMOS line-scan camera. We have shown that the sensitivity performance of this instrument is comparable with a system using a CCD detector if the signal loss in the optical and fiber optics elements is minimized. The design of the instrument allows for high flexibility in selection of imaging modes, ranging from high resolution and high definition two dimensional imaging to ultrahigh speed acquisition of time sequences of three dimensional data. No changes in the configuration of the optics, just in the control software settings, are necessary to switch between the different imaging protocols.

The instrument has an axial resolution of 6.9 μm and an imaging depth of 5.2 mm. Application of complex conjugate image removal technique based on the joint Spectral and

#106214 - $15.00 USD Received 12 Jan 2009; revised 6 Mar 2009; accepted 8 Mar 2009; published 12 Mar 2009

Time domain OCT method enabled to double the axial imaging range, allowing to image the entire anterior segment of the eye from the apex of the cornea to the posterior apex of the crystalline lens.

We have demonstrated imaging of the specific structures in the anterior chamber including the anterior chamber angle and the entire crystalline lens, at 800 nm. Adequate protocols have allowed us obtaining images of the iridocorneal angle, despite high attenuation of light by the sclera, of similar quality to those previously demonstrated at 1300 nm [38]. Additionally higher scattering of 800 nm light comparing to 1300 nm enables visualization of internal structure of the crystalline lens in young and healthy subjects.

High-speed signal detection enabled us to perform *in vivo* studies of dynamic processes in the anterior chamber. We have presented volumetric real time tomographic movies showing eye blinking and pupil reaction to white-light stimulus. Finally, we have demonstrated for the first time OCT imaging of the crystalline lens dynamics during accommodation.

We believe that the instrumentation described here will allow for a wide range of new applications including basic research of mechanical properties of cornea, limbus, iris and lens. Future imaging of static and dynamic properties of ocular tissues may provide important qualitative and quantitative information about the optics and biomechanics of the optical system of eye.

Acknowledgments

This work was supported by EuroHORCs-European Science Foundation EURYI Award EURYI-01/2008-PL (M.W.) and EURYI-05-102-ES (S. M.) as well as by Polish Ministry of Science and Higher Education (research grant for years 2006-2008) and by the project operated within the Foundation for Polish Science Ventures Programme co-financed by the EU European Regional Development Fund (M. G.). The support of the Rector of the Nicolaus Copernicus University (scientific grant 504-F M.W.) is also gratefully acknowledged. We would like to acknowledge our collaborators: Laura Remon, Damian Siedlecki and Carlos Dorronsoro. Special thanks to dr Bartłomiej Kałużny from Collegium Medicum UMK for his support. We would like to kindly acknowledge help of Tomasz Bajraszewski, Paweł Wojdas, Paweł Staniszewski and Grzegorz Bednarczyk from Optopol Technology S. A.

#106214 - $15.00 USD Received 12 Jan 2009; revised 6 Mar 2009; accepted 8 Mar 2009; published 12 Mar 2009